Open Sys. & Information Dyn. **4**: 407–434, 1997

Chaos in Semiconductor Microstructures

Henrik Bruus*
Applied Physics, Yale University, P.O.Box 208284, New Haven, CT 06520-8284, U.S.A.

(Received: May 30, 1996)

Abstract. Some main experimental and theoretical aspects of chaos in semiconductor microstructures are reviewed in these lecture notes. The lecture, which is meant for non-specialists, evolves from a general introduction to basic concepts of semiconductor microstructures, through a presentation of various studies of chaos in these structures, to a more thorough discussion of the specific topic of how to probe quantum chaos with deformable semiconductor quantum dots. Only broad outlines and simplified arguments are used to explain the central ideas.

1. Introduction

The relevance of concepts from the theory of "quantum chaos" to mesoscopic physics has become increasingly clear as microstructure technology has achieved controlled fabrication of systems smaller than both the elastic and inelastic scattering length [1]. Quantum chaos is the generally accepted term for properties of a quantum system associated with classical chaos or with the classical transition to chaos. In the most recent high-mobility semiconductor microstructures transport is ballistic and the dominant scattering mechanism is the reflection of the electrons at the boundaries of the structure which, depending on the nature of the confining potential, may generate classically chaotic, mixed or integrable dynamics. Thus they present experimental possibilities for the application and testing of concepts from the theory of quantum chaos in condensed matter physics. Disordered mesoscopic systems also are, no doubt, classically chaotic, and recent work has emphasized the similarity between disordered quantum systems and the ballistic systems which have chaotic boundary scattering. In particular, at low temperature both types of systems exhibit sample-specific mesoscopic fluctuations in various physical properties as a function of external parameters such as magnetic field. The ballistic systems differ from the disordered ones however in two ways. First, as we will use the term, a disordered system generates elastic scattering of electrons on a scale L_e which is short compared to typical sample dimensions L. This means that transport is diffusive on a scale smaller than the system size, and because the diffusion process is dependent on dimensionality, the statistical properties depend in general on the spatial dimension. Chaotic ballistic systems on the other hand have no relevant transport length smaller than the system size and thus many of their properties are insensitive to the spatial dimensionality and they are said to be "quasi-zero-dimensional". It turns out that this difference leads to differences in the statistical properties of disordered and chaotic systems in certain regimes of

*Present address: Niels Bohr Institute, Blegdamsvej 17, DK-2100 Copenhagen Ø, Denmark (email: bruus@nbi.dk)

energy and temperature [2, 3]. Second, there is reasonable evidence that ballistic systems may be fabricated with geometries and potential profiles which generate nearly integrable classical dynamics, thus it becomes worthwhile to consider models which describe the transition to chaos and not just fully chaotic dynamics.

There are two main approaches to the quantum theory of chaotic systems. The approach through semiclassical quantum mechanics pioneered by Gutzwiller [4], and the approach based on the random matrix theory [5] first applied to quantum chaos by Bohigas, Giannoni and Schmit [6]. The former approach makes a more direct connection to the classical mechanics and has recently had major successes recently in atomic physics. However the confining potential in the microstructures studied experimentally is seldom known well enough to justify theoretical work relying on specific classical orbits. Instead, either a wholly statistical approach, or a combination of semiclassical and statistical ideas have been applied to quantum chaos in mesoscopic systems. Three measured physical effects which have been proposed as manifestations of quantum chaos in mesoscopic transport are: 1) The resistance fluctuations in GaAs quantum wires coupled strongly to an electron cavity [1, 7, 8, 9]. 2) The weak localization effect in the same system [9, 10] 3) The fluctuations in the Coulomb blockade conductance peaks [11, 12] in quantum dots weakly coupled to leads [13, 14, 15, 16, 17]. The electron cavity conductance fluctuations have been described by a combination of statistical and semiclassical theory, and most recently certain properties have been derived from random-matrix theory [18, 19], whereas the Coulomb blockade peak fluctuations in quantum dots have been completely described statistically, using only random-matrix theory. The quantum dot conduction experiments are analogous to strongly resonant scattering in atoms or nuclei for which the properties of a single quasi-bound state can be probed. In micron-size semiconductor quantum dots at the typical experimental density it is estimated that the single-particle level-spacing (or the excitation energy to the first excited state) $\Delta\varepsilon \sim 0.05$ meV ~ 500 mK. and therefore these systems may be studied in the regime $kT < \Delta\varepsilon$, where indeed only a single quasi-bound state participates in the resonance.

The paper is organized as follows. In Section 2, a brief overview is given of the fabrication of semiconductor microstructures and of the basic transport measurements. We discuss the macroscopic regime at high temperatures (T is between $\approx$ 50 K and room temperature), where the size L of the devices is larger than any of the microscopic lengths, such as the elastic free mean path L_ℓ (the distance the electrons move between two successive elastic scattering events) and the phase coherence length L_ϕ; in short: $L_\phi, L_\ell \ll L$. In this regime the conduction electrons move diffusively; they behave as classical billiard balls performing a random walk due to the elastic scattering against impurities in the material.

In Section 3 the phase coherence length, L_ϕ, of the electrons is introduced. Roughly speaking L_ϕ, is the length scale over which the electrons maintain their quantum mechanical wave nature (their phase) before losing it in the scattering processes. A discussion is then given of two very important quantum effects in resistance measurements in the macroscopic regime at low temperatures ($T \approx 1$ K and $L_\ell < L_\phi < L$): *weak localization* and *Aharonov-Bohm oscillations*.

In Section 4 the mesoscopic regime is introduced as the regime where the sample size L is smaller than or comparable to L_ϕ but still larger than L_ℓ ($L_\ell < L < L_\phi$).

The main characteristics of this regime is the appearance of sample specific random but still reproducible, resistance fluctuations — the so called *universal conductance fluctuations*.

In Section 5, we move on to the ballistic regime, where the sample size becomes the smallest length scale ($L < L_e < L_\phi$). This regime is where we expect to find quantum chaos since the scattering is now dominated by specular reflections of the walls of the system and because the electrons maintain their quantum mechanical phase coherence during many bounces inside the system. Current experimental and theoretical work on conductance fluctuations and weak localization is discussed.

In Section 6, we study in more detail a specific example of quantum chaos in a condensed matter system: quantum chaos in a deformable quantum dot. This is the result of recent work presented here to give the student a flavor of new directions within the field of quantum chaos in semiconductor microstructures. Finally, in Section 7, we present concluding remarks.

2. Device Fabrication and Basic Experiments

To be able to perform studies of quantum chaos in condensed matter systems it is indispensable to manufacture systems where the conduction electrons have very long mean free paths. Long mean free paths mean that the electrons can move over long distances inside the device without scattering against impurities. The best and the most widely used system today to obtain this situation is the GaAs/$Ga_{1-x}Al_xAs$ heterostructure in which the motion of the conduction electrons is confined to a 2-dimensional plane near the interface between the GaAs and the $Ga_{1-x}Al_xAs$ interface. The reduction of dimensionality from 3 to 2 reduces the effect of scattering significantly. For example the (low temperature) elastic mean free path L_e in 3D GaAs is of the order 0.1 μm , whereas it can be as high as 10 μm in the 2D electron gas of the heterostructure.

2.1. The GaAs/$Ga_{1-x}Al_xAs$ heterostructure

The first GaAs/$Ga_{1-x}Al_xAs$ heterostructure was created in 1979 and the existence of a 2-dimensional electron gas (2DEG) in it was demonstrated [20]. Since then the 2DEGs has played a central role in the investigation of quantum effects in electron transport, e.g. the fractional quantum Hall [21] and the quantization of conductance [22] was discovered in 2DEGs in GaAs-based heterostructures.

The GaAs/$Ga_{1-x}Al_xAs$ heterostructure can be fabricated by using molecular beam epitaxy. On top of a conventionally grown GaAs substrate the heterostructure is grown atomic layer by atomic layer in an ultra high vacuum chamber. Beams of various molecules each containing either Ga, Al, or As is directed towards the substrate which, in order to obtain the most uniform and perfect crystal, is rotating and kept at an elevated temperature (several hundred degrees centigrade) during growth. The growth rate is about one atomic layer per second and it is possible to change the chemical composition abruptly from one layer to the next. The GaAs crystal and the $Ga_{1-x}Al_xAs$ crystal (where a fraction x, typically 30 %, of the Ga atoms are substituted with Al atoms) have the same crystal structure (the zinc-blende structure) and almost the same lattice constant (distance between the

atoms). Therefore, it is possible to grow very stable heterostructures without any significant mechanical strain at the interface. The two crystals are both semiconductors. That means that at very low temperatures almost all electrons have left the conduction band and gone down to the valence band leaving the system in an insulating state. To ensure that a sufficient number of conduction electrons are present even at the lowest temperatures, a part of the $Ga_{1-x}Al_xAs$ crystal is doped with Si atoms. Each of these atoms can give off one electron to the conduction band (hence their name: donors) and the crystal therefore remains able to conduct electrical currents at low temperatures. A crucial feature which allows very long mean free paths is the placement of the Si donors relatively far away from the interface where the electrons move around. By growing a layer (the so called spacer layer) of pure $Ga_{1-x}Al_xAs$ typically 10 nm thick immediately after the interface, and only thereafter starting to dope with Si, the resulting potential from the donors at the position of the 2DEG is very smooth and scattering due to the ionized donors is minimal. A typical heterostructure containing a 2DEG 65 nm below the surface is shown in Tab. 1.

10 nm thick	Cap layer	GaAs:Si	N+ doped (2×10^{24}Si/m^3)
35 nm thick	donor layer	$Ga_{0.72}Al_{0.28}As$:Si	N+ doped (2×10^{24}Si/m^3)
15 nm thick	spacer layer	$Ga_{0.72}Al_{0.28}As$	undoped
1 μm	buffer layer	GaAs	P unintentionally doped
630 μm	substrate	GaAs (LEC)	undoped

Tab. 1. A typical GaAs/$Ga_{1-x}Al_xAs$ heterostructure. The mean free path at 4 K is 10 μm, the electron density is 4.2×10^{15} m^{-2}, and the mobility (an often quoted figure of merit) is 100 T^{-1}. A 2-dimensional electron gas is formed in the undoped GaAs layer close to the undoped GaAlAs layer.

The 2DEG is formed because the conduction electrons in $Ga_{1-x}Al_xAs$ have a higher energy than in GaAs in spite of the similarity of the crystal structures. The electrons are therefore transferred to the GaAs. However, since the positively charged Si donors, from where the electrons originated, are immobile and remain in the $Ga_{1-x}Al_xAs$ crystal, the electrons in the GaAs crystal are bound close to the interface by electrostatic forces. The effective potential experienced by the electrons in the direction perpendicular to the interface (the z direction) is shown in Fig. 1. It is seen that the electrons move in a very narrow triangular potential well only about 10 nm wide. This is only 100 times the diameter of the Hydrogen atom. Consequently a large size-quantization is present. It turns out that the energy difference $E_1 - E_0$ between the electron state with zero nodes in the z part of the wave function (ζ_0) and one node (ζ_1) is about 10 meV corresponding to a thermal energy at 100 K. It is therefore clear that at temperatures near 1 K all electrons will be in the lowest (zero node) state and stay there. Any change of the electronic wave functions in the z direction is prohibited and hence no movement in that direction is possible. In the plane parallel to the interface the electrons can move freely. It is in this sense we talk about a 2-dimensional system or 2DEG.

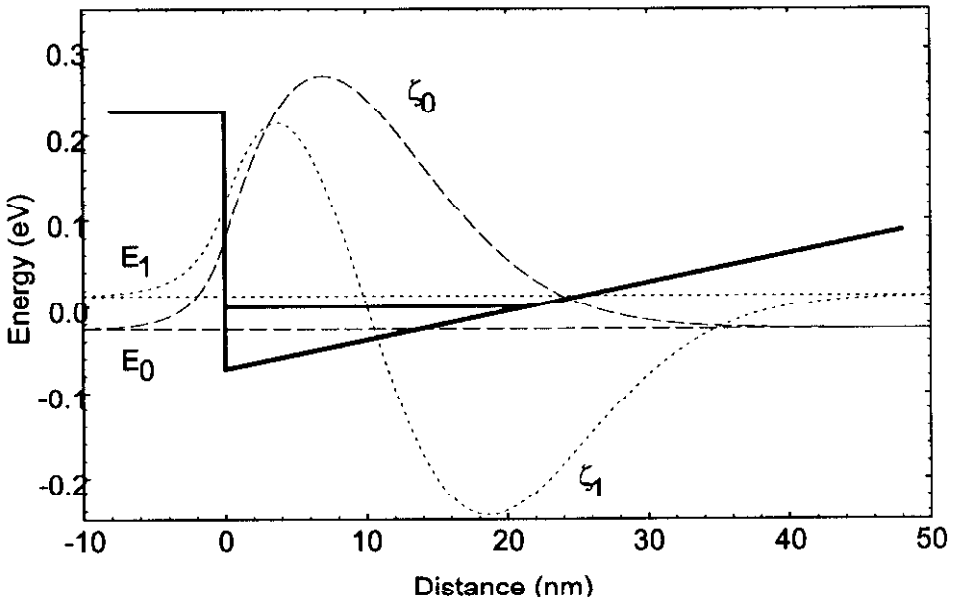

Fig. 1. The band structure in the z direction perpendicular to the interface between the GaAlAs layer ($z < 0$) and the GaAs layer ($z > 0$) in a GaAs heterojunction. The effective triangular potential well giving rise to the 2DEG is shown. The Fermi energy is indicated by the horizontal straight full line inside the well. The ground state energy E_0 is indicated by the long dashed straight line, and the corresponding (envelope) wave function ζ_0 is given by the dashed curve. Likewise the first exited state ζ_1 and its energy E_1 is indicated by the dotted lines. More details are given in [30].

2.2. Resistance measurements on a 2DEG

To be able to make well defined measurements of the electrical transport properties of the 2DEG we want to make a device which, for example, allows us to measure the longitudinal resistance as well as the Hall resistance. A generic device, a so called Hall bar, for such measurements is shown in Fig. 2. Let $V_{ij} = \mu_i - \mu_j$ denote the voltage difference measured between contact i and j and let I_{kl} denote the current flowing between contact k and l. Resistances are defined as:

$$R_{ij,kl} \equiv \frac{V_{ij}}{I_{kl}}. \tag{1}$$

An example of a longitudinal resistance could then be $R_{23,14}$ and of a Hall resistance $R_{26,14}$. It is in anticipation of the discussion of the phenomena in the mesoscopic regime that we deal with resistances and specification of measurement procedures rather than the notion of intrinsic resistivities.

To fabricate a Hall bar in a 2DEG some processing of the heterostucture is needed. This is sketched in Fig. 3. First a mask containing the geometrical shape of the device is made by photographic techniques. Next a layer of photoresist is spun

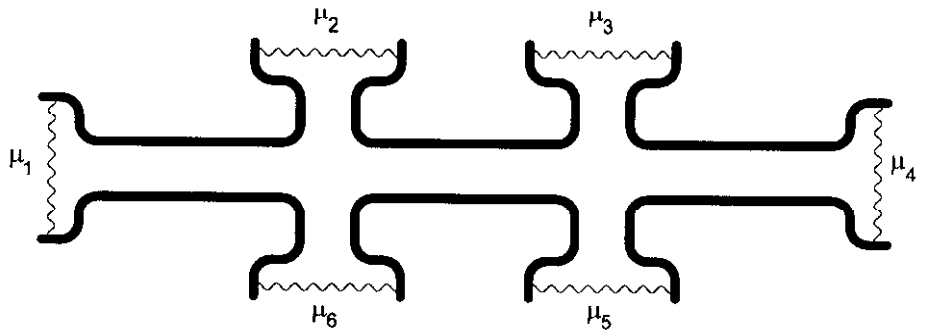

Fig. 2. A typical Hall bar geometry used in transport measurements. Contacts 1 and 4 are often used as current contacts while contacts 2, 3, 5, and 6 are used as voltage probes. The wavy lines mark the borderline between the sample containing a perfect 2DEG and the ohmic contacts (known as electron reservoirs) each with a electro-chemical potential μ_j.

over the heterojunction. The mask is then placed on top of the heterojunction and the system is exposed to ultra-violet light. Where the mask protects the photoresist nothing happens, but where the resist is exposed to the UV-light it breaks down. After illumination the heterojunction is placed in a chemical active liquid which dissolves and removes the irradiated part of the resist. Finally, the heterojunction is placed in an acid which etches away the unprotected part of the surface but leaves the structure underneath the undissolved resist intact. As a result we are left with a heterojunction containing a 2DEG shaped as the original photo mask. Using this method the smallest features that can be made is of the order of 1 μm . Finer details down to the size of about 0.01 μm can be made by using a sharply focused electron beam instead of UV-light to write on the resist. This finer scale will be of crucial importance in Section 5, where we want to study effects in the mesoscopic regime. To make electrical contacts to the 2DEG one last process step is necessary. Through a new mask metal atoms (mostly Au, Ge, and Ni) are evaporated to the six contact areas shown in Fig. 2. After evaporation the mask is removed and the whole device is placed in an oven where it is heated until enough metal atoms have diffused from the surface down to make contact to the 2DEG. It is now possible to attach wires to the metal pads on the surface enabling resistance measurements of the 2DEG.

3. Quantum Effects in Low Temperature Resistance Measurements

In the standard Drude theory of the resistance R in a 2DEG of width W, length L, and electron density n, all temperature dependence is contained in the scattering time τ (the typical time between scattering processes).

$$R = \frac{L}{W}\frac{m}{ne^2}\frac{1}{\tau}. \tag{2}$$

At high temperatures the scattering is dominated by inelastic processes (electron-phonon scattering). As the temperature is lowered the lattice vibrations die out

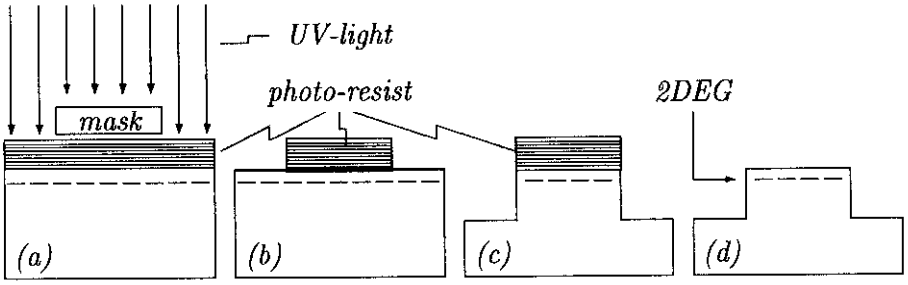

Fig. 3. A sketch of the four process steps in the device fabrication. (a) Photoresist is exposed to UV-light outside the mask. (b) Exposed photo resist is removed. (c) Etching of the heterojunction where it is not protected by resist. (d) Removal of the resist.

leading to a decrease in the resistance. The decrease stops at low temperature, where the temperature independent elastic scattering processes involving stationary lattice defects dominate. This scattering is characterized by the elastical mean free path L_e which the electrons travel between scattering events. In macroscopic samples the mean free path $L_e < L, W$ and we are in the diffusive regime illustrated in Fig. 4a.

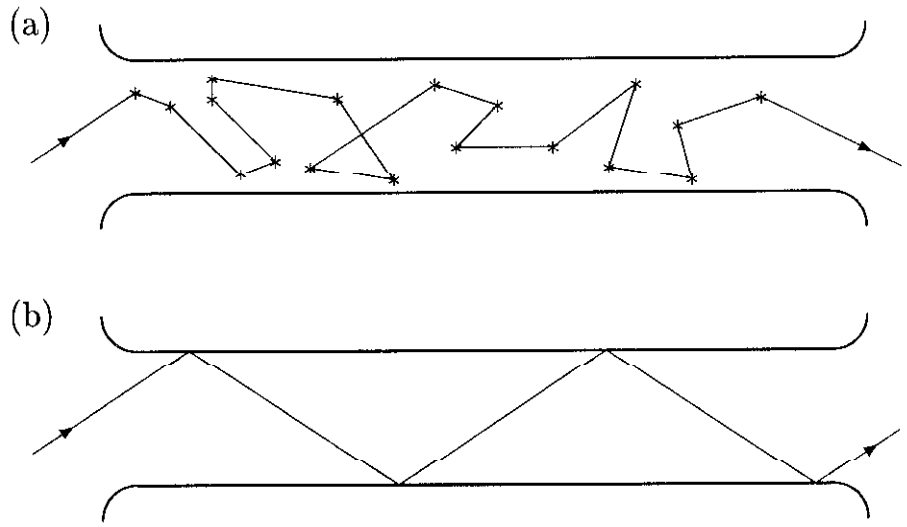

Fig. 4. Illustration of a sample of length L and width W in the (a) the diffusive regime where $L_\phi \ll L_e \ll L, W$ and (b) the ballistic regime where $L, W \ll L_\phi, L_e$.

At low temperatures the 2DEG is described in terms of a degenerate Fermi gas. Therefore, the only electrons responsible for the electrical transport properties are the ones with energies ε near the Fermi energy ε_F corresponding to a velocity v_F, the Fermi velocity. On length scales larger than L_e the diffusion is governed by

the classical diffusion equation which connects gradients in the electron density n with the flow of particles $\mathbf{j}$ (equal to $n\mathbf{v}$):

$$\mathbf{j} = -D\boldsymbol{\nabla} n\,, \tag{3}$$

where D is the diffusion constant. Differences δn in the density are typically decaying on the length scale L_e, while typical currents are of the order $\delta n\, v_F$. Hence, we have the following estimate $\delta n\, v_F \approx D\delta n/L_e$ so that $D \approx v_F L_e$. An accurate calculation yields

$$D = \frac{1}{2} v_F L_e\,. \tag{4}$$

Now, imagine that at time $t = 0$ a number of electrons N are placed at the point $\mathbf{r}_0$. Solving (3) using the continuity equation, $\boldsymbol{\nabla}\cdot\mathbf{j} = -\frac{\partial n}{\partial t}$, yields the following solution for the resulting density, $n(\mathbf{r}, t)$, as a function of space and time:

$$n(\mathbf{r}, t) = \frac{N}{2\pi D t} \exp\left(-\frac{(\mathbf{r}-\mathbf{r}_0)^2}{2Dt}\right). \tag{5}$$

The electrical conductance, $G = 1/R$ (the inverse of the resistance), is connected to the diffusion process through the Einstein relation

$$G = \frac{e^2}{h}\frac{W}{L}\frac{2mD}{\hbar}\,, \tag{6}$$

where e^2/h is the quantum unit of conductance to be encountered often in the following.

3.1. Weak localization in the diffusive regime

The Drude theory neglects the quantum mechanical wave nature of the electrons between scattering events (which themselves are treated quantum mechanically). At high temperatures this is an accurate description because electron-electron and electron-phonon scattering destroys phase coherence of the electron waves on a length scale L_ϕ (the phase coherence length) which is much shorter than L_e. As the temperature is lowered below ~70 K the phonons becomes unimportant, while the electron-electron scattering still breaks the phase coherence significantly down to ~4 K. Below 4 K, however, L_ϕ becomes comparable to and even larger than L_e. In this regime, an increase in the otherwise constant residual resistance occurs. This effect, known as *weak localization* [24, 25, 26, 27], is due to quantum interference effects, and consequently it cannot be treated in the Drude theory.

To understand the effect qualitatively we use the Feynman path integral formulation of quantum mechanics. According to this formulation, the probability $P(\mathbf{r}_1, \mathbf{r}_2)$ of going from point $\mathbf{r}_1$ to point $\mathbf{r}_2$ is found by taking the absolute square of the sum over all possible paths j leading from $\mathbf{r}_1$ to $\mathbf{r}_2$ of the probability amplitudes A_j of each path. The A_j's are complex numbers given by $A_j = \sqrt{P_j}e^{i\phi_j}$, where P_j is the classical probability for path j and where ϕ_j is the quantum phase an electron acquires by traversing path j,

$$P(\mathbf{r}_1, \mathbf{r}_2) = \Big|\sum_j A_j\Big|^2 = \sum_{j=k}|A_j|^2 + \sum_{j\neq k} A_j A_k^* = \sum_j P_j + \sum_{j\neq k}\sqrt{P_j P_k}e^{i(\phi_j-\phi_k)}\,. \tag{7}$$

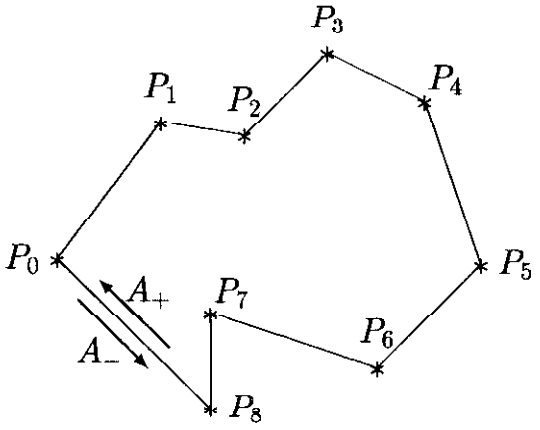

Fig. 5. A closed loop traversed clockwise, A_+, and counterclockwise, A_-, by a particle in the regime where $L_\phi > L_e$.

The first term in the result above is just the classical probability for the process. The second term contains interference between different paths. Normally these interferences average to zero due to the randomness of the large number of phases and due to phase breaking processes. However, in the limit $L_\phi > L_e$ a certain class of interference does not vanish. If we consider the probability $P(\mathbf{r}_1, \mathbf{r}_1)$ of returning to the starting point $\mathbf{r}_1$ we note that a given closed loop, as illustrated in Fig. 5, can be traversed both clockwise, with amplitude A_+, and counterclockwise, with amplitude A_-. Since such a pair of paths are identical except for the direction of traversal, the two phases, ϕ_+ and ϕ_-, are identical and the cross term $\sqrt{P_+P_-}e^{i(\phi_+ - \phi_-)} = P_+ = P_-$ does not vanish upon averaging. Thus, all closed loops give rise to a correction to the classical probability of returning to the starting point. This of course affects the diffusion. A negative correction δD to the diffusion constant D appears because of the enhanced probability for an electron to return to its point of injection. The relative correction $(\delta D)/D$ can be estimated as follows. The probability for one electron to return to within the infinitesimal area d^2r of the starting point in time t is found from (5) by setting $N = 1$, $\mathbf{r} = \mathbf{r}_0$ and multiplying with $d^2r = k_F^{-1} v_F dt = 2\hbar/m$, k_F^{-1} being the width of the wave packet and $v_F dt$ the distance it covers in the time step dt. This probability is then multiplied by the probability $(1 - e^{-t/\tau})$ for an electron to scatter at least once (enabling it to return) and by the probability $(1 - e^{-t/\tau_\phi})$ for an electron to stay phase coherent in the time interval t. Finally, an integral over time is performed,

$$\frac{\delta G}{G} = \frac{\delta D}{D} = -\int_0^\infty \frac{2\hbar}{m} dt \frac{1}{2\pi D t}(1 - e^{-t/\tau})(1 - e^{-t/\tau_\phi}) = \frac{\hbar}{2\pi m D} \ln\left(1 + \frac{\tau_\phi}{\tau}\right). \quad (8)$$

The weak localization effect can be suppressed by an external magnetic field B. This suppression follows from basic quantum mechanics according to which an electron picks up an extra phase $+BSe/\hbar$ when it completes clockwise a closed loop

enclosing the area S. The sign changes under counterclockwise motion. Therefore, when B is present the phases of A_+ and A_- no longer cancel and interference begins to play a role. Suppression of the weak localization sets in at a critical magnetic field B_c when the phase difference $2B_cSe/\hbar$ for the time-reversed paths enclosing the typical area $S = L_\phi^2$ is of the order 1. We therefore find $B_c \sim h/eL_\phi^2$. This effect gives a method to measure L_ϕ: measure conductance as a function of B and estimate the field B_c at which the weak localization begins to be suppressed. Then calculate $L_\phi \sim \sqrt{\hbar/eB_c}$.

3.2. Aharonov-Bohm oscillations with period $h/2e$

A more dramatic dependence on B is seen in 3D-cylinders. In the famous experiment by Sharvin and Sharvin [28] a 1 cm long Li cylinder of radius 1.1 μm and wall thickness 0.12 μm was placed in a magnetic field parallel to its axis. Electrons were injected at one end and extracted at the other end. In this sample L_ϕ is 2.3 μm. Hence, phase coherence all the way along the cylinder is impossible. However, phase coherence around the cylinder is possible [29]. Because of the geometry all loops around the cylinder enclose almost the same area S_0 and the same magnetic flux. Hence, superimposed on the general suppression of the weak localization clear oscillations are seen with a period ΔB determined by the requirement that the phase difference $2\Delta BS_0e/\hbar$ between clockwise and anticlockwise moving electrons is 2π, i.e. $\Delta B = h/2eS_0$. Often magnetic flux Φ ($= B \times$ area) is used as variable instead of B. Thus the flux period $\Delta\Phi = \Delta BS_0 = h/2e$, and hence the name *$h/2e$-oscillations.*

4. Mesoscopic Physics

We now move on to study the regime where $L_e < L, W < L_\phi$, which allows the electrons to stay phase coherent through the entire sample. A typical path still looks like the one shown in Fig. 4a, but now the quantum phases are maintained along the path. The pronounced wave-like behavior of the electrons makes it natural to discuss electron transport in the wave guide picture of Landauer and Büttiker [30, 31]. The electrons are emitted into the system from completely phase randomizing electron reservoirs (the contacts) through perfect leads which does not reflect any electron waves and which allows an identification of electronic wave modes denoted α and/or β in the following. As an example α could be the number of nodes in the transverse wave function. Conductance, $G = 1/R$, is then calculated as

$$G = \frac{2e^2}{h} \sum_{\alpha,\beta} |t_{\alpha\beta}|^2 , \tag{9}$$

where $t_{\alpha\beta}$ is the quantum mechanical transmission probability amplitude from the incoming mode α to the outgoing mode β (the factor 2 is due to spin).

4.1. Quantization of the conductance G

A simple but very important example of how this picture works is the quantum point contact experiment [22]. A 2DEG shaped as a simple straight transmission line is partly blocked at the midpoint by a saddle shaped potential generated by negatively charged metal gates coming in from the sides on the top of the structure. At large negative bias the opening is very narrow blocking all transmission through the device, and G is zero. As the bias is brought up towards zero the opening widens, the energy bound in the transverse motion lowers, and at some point the mode with zero nodes in the transverse wave function have enough longitudinal energy to pass the saddle shaped constriction. The transmission for going from the 0-node mode on the left to the 0-mode mode on the right becomes 1 and G jumps from zero to $2e^2/h$. For slightly higher gate voltages the 1-node mode can also pass and G jumps to $4e^2/h$, and so forth. This explains the beautiful staircase-like graph of the conductance plotted versus gate voltage seen experimentally.

4.2. Universal conductance fluctuations

In the mesoscopic regime the conductance fluctuates significantly between individual members of an ensemble of macroscopically identical samples and as a function of magnetic field or Fermi energy. The ergodic hypothesis [32] states that averages over external parameters are the same as sample averages. The phase coherence is maintained on the length scale L_ϕ which is comparable to or larger than the device size L, so in contrast to the classical case, where the root-mean-square fluctuations δG typically is smaller than the average conductance $\langle G\rangle$ by a factor $\sqrt{L_e/L} \ll 1$, δG remains non-negligible here. In fact, it was discovered a decade ago [32, 33, 34] that in the mesoscopic regime the conductance fluctuations are universal, the variance of the fluctuations are roughly e^2/h independent of L and $\langle G\rangle$ and only weakly dependent on geometry. A simple argument due to Lee [35] gives an insight to the effect. Instead of using transmission probabilities $|t_{\alpha\beta}|^2$ as in (9), the reflection probabilities $|r_{\alpha\beta}|^2$ are used. The r's and t's are connected by current conservation: $\sum|t|^2 = N - \sum|r|^2$, where N is the number of channels. The variance of the conductance can now be expressed as $\mathrm{Var}(G) = (e^2/h)^2\mathrm{Var}(\sum|r|^2) = (e^2/h)^2N^2\mathrm{Var}(|r|^2)$, where we have used that the r's are independent of each other (this is not true for the t's which is why the r's are studied). To calculate $\mathrm{Var}(|r|^2) = \langle|r|^4\rangle - \langle|r|^2\rangle^2$ we introduce the amplitude A_i for path i through the system. This is a meaningful concept due to the global phase coherence in the mesoscopic regime. We find $\langle|r|^4\rangle = \sum\langle A^*(i)A(j)A^*(k)A(l)\rangle \approx 2\sum\langle|A(i)|^2|A(k)|^2\delta_{ij}\delta_{kl}\rangle = 2\langle|r|^2\rangle^2$. As a result we have $\mathrm{Var}(|r|^2) = \langle|r|^2\rangle^2$. Since $\langle|r|^2\rangle \approx 1/N$ we finally obtain $\delta G = \sqrt{\mathrm{Var}(G)} = e^2/h$. Another result of the analysis is that the fluctuation pattern can be completely rearranged by moving just a few impurities. This reflects the global phase coherence in the system.

4.3. Aharonov-Bohm oscillations with period h/e

The last example of a mesoscopic effect is the Aharonov-Bohm effect in a flat mesoscopic gold ring in a perpendicular magnetic field measured by Washburn et

al. [36]. The diameter of the ring is 825 nm in diameter, while the thickness is less than 100 nm. In contrast to the long cylinder mentioned in Section 3.2 the electrons maintain their phase coherence globally in the flat ring. As a result, interference between electron waves propagating through the left and the right side of the ring occurs. The minimal area thus enclosed by phase coherent electrons is equal to the area S enclosed by the ring. Like in the cylinder we can also consider electrons going all the way round clockwise and counterclockwise resulting in an effective area of $2S$. In the flat ring we therefore observe both h/e and $h/2e$ oscillations.

5. Quantum Chaos in Open Microstructures

The last regime to be treated in this overview is the ballistic regime characterized by the inequalities $L, W < L_\epsilon, L_\phi$ (see Fig. 4b). In this regime, single electrons move coherently through the sample and the dominant scattering is collision with the walls of the sample.

5.1. The ballistic regime

Some of the first direct experimental proof of the existence of the ballistic regime came from studies of the Hall effect in narrow wires. In mesoscopic Hall bars it was found that the Hall effect was quenched in narrow wires. The electrons shoot past the Hall probes without deflection and no Hall voltage is measured. By changing the sharp 90° corners of the Hall bar to soft slanted corners it is even possible to reverse the sign of the Hall voltage. The electrons are deflected slightly upward by the magnetic field but a majority hits the slanted wall and are reflected into the opposite voltage probe. A Hall voltage with the "wrong" sign results [37].

5.2. Quantum chaotic scattering

The existence of ballistic transport in semiconductor microstructures at low temperatures makes it possible to use these systems for testing theoretical concepts developed in the study of quantum chaotic scattering. A generic example of how such experiments are performed is the experiment by Marcus et al. [38]. A metal gate structure is evaporated on the surface of a heterojunction. When the gate is charged negatively the resulting confinement potential expels the 2DEG away from the gate region and the 2DEG is forced into the shape of the gate. In this example two devices are made, one shaped as a circle and the other as a stadium. The circular device ought to generate integrable motion and the stadium chaotic motion. Several questions can be addressed in such systems, e.g. how do the statistical properties of the conductance in the chaotic shape differ from those in the integrable (or nearly integrable) shape? And can the quantum interference effects be related to properties of the corresponding classical system? In the following we will provide partial answers to these questions.

As before a good starting point for calculating the conductance is (9). The transmission coefficients $t_{\alpha\beta}$ is given by

$$t_{\alpha\beta} = -ih\sqrt{v_\alpha v_\beta}\int dy \int dy' \phi_\alpha^*(y')\phi_\beta(y) G(y', y', \varepsilon_F)\,, \tag{10}$$

where v_α (v_β) and $\phi_\alpha(y')$ ($\phi_\beta(y)$) are the longitudinal velocity and transverse wave function for the mode α (β). G is the retarded Green's function between points (x, y) on the left lead and (x', y') on the right lead. Exact (numerical) calculations of $t_{\alpha\beta}$ can be performed using the recursive Green's function technique [39]. Analytical results can be obtained by using the semiclassical method [7] where $G(y', y, \varepsilon_F)$ is approximated by its semiclassical path-integral expression [4],

$$G(y', y, \varepsilon_F) \simeq \frac{2\pi}{(2\pi i\hbar)^{3/2}} \sum_{s(y,y')} \sqrt{D_s} \exp\left(\frac{i}{\hbar} S_s(y', y, \varepsilon_F) - i\frac{\pi}{2}\mu_s\right), \qquad (11)$$

where S_s is the action integral along the *classical* path s, at energy ε_F, $D_s = (v\cos\theta'/m)^{-1} \times |(\partial\theta/\partial y')_y|$, θ and θ' are the incoming and outgoing angles, and μ is the Maslov index. After inserting (11) in (10) $t_{\alpha\beta}$ can be calculated using the method of steepest descent. The result is a sum over classical paths through the system over a quantity depending only on classical parameters.

5.3. Conductance fluctuations in the ballistic regime

Jalabert et al. [7] studied the correlation function $C(\Delta B) = \langle \delta G(B) \delta g(B + \Delta B) \rangle$ of the magnetoconductance for weak fields theoretically and Marcus et al. [38] studied it experimentally using the devices mentioned in Section 5.2. Here the important quantity is the phase difference $\Delta\phi$ between the phase of the classical path s at B and the same path at $B + \Delta B$: $\Delta\phi = \Delta S_s/\hbar \simeq \frac{1}{\hbar}\frac{\partial S}{\partial B}\Delta B$. This allows us to define a generalized area A given by $\Delta\phi \equiv 2\pi A \Delta B/(h/e)$. In the chaotic case the electrons sweep out areas like in a random walk. The root-mean-squared area α_{cl}^{-1}, which is a purely classical entity, shows up in the distribution $P(A)$ of areas: $P(A) \propto \exp(-2\pi\alpha_{cl}|A|)$. This distribution is then used to calculate the sum over classical paths mentioned above, and the final result for $C(\Delta B)$ is:

$$C(\Delta B) = \frac{C(0)}{[1 + (\Delta B e/\alpha_{cl} h)^2]^2}. \qquad (12)$$

To compare with experiment we calculate the Fourier transform $S_g(f)$ of $C(\Delta B)$ and obtain

$$S_g(f) \equiv \mathcal{F}(C(\Delta B)) = S_g(0)\,[1 + (2\pi\alpha_{cl} h/e) f] \exp(-(2\pi\alpha_{cl} h/e) f). \qquad (13)$$

The theoretical $S_g(f)$ agrees with experimental one over three orders of magnitude. Furthermore, the extracted values, 0.87 μm $^{-2}$ and 0.94 μm $^{-2}$, of α_{cl} for two different realizations of the same stadium is in rough agreement with simulations (0.62 μm $^{-2}$) and simple analytical work based on escape probabilities (0.76 μm $^{-2}$). Finally, the power spectrum of the circle has more weight at higher "areas" B^{-1}. This is expected since a particle moving in a circular cavity accumulates area linearly in time, $A(t) \sim t$, whereas in the chaotic case the process is diffusive, $A(t) \sim \sqrt{t}$. An enhanced large area content is therefore expected for the circle.

5.4. Weak localization in the ballistic regime

A second example of quantum chaos versus integrability in microstructures is the weak localization. In Section 3.1, we discussed how weak localization occurred

in the diffusive regime due to coherent backscattering from impurities. A similar effect occurs in the ballistic regime due to coherent backscattering from the walls. A semiclassical treatment analogous to the one mentioned above yields the following result for the ensemble averaged weak localization correction $\langle \delta R \rangle$ to the resistance:

$$\langle \delta R \rangle \propto 1/[1 + (2Be/\alpha_{cl}h)^2], \qquad \text{chaotic shapes}, \tag{14}$$

$$\langle \delta R \rangle \propto -|B|, \qquad \text{integrable shapes}. \tag{15}$$

In the diffusive regime where $L_\phi \ll L$ the weak localization is an average over many cells of size $L_\phi \times L_\phi$ and therefore the effect is clear. In the ballistic regime no such (self-) average is performed since $L_\phi > L$, and the effect is therefore masked by the universal conductance fluctuations. It is not possible to enlarge the sample to obtain self-averaging because then we are no longer in the ballistic regime. To obtain an unambiguous weak localization effect it is therefore necessary to make a real sample average. Such an experiment has recently been carried out by Chang et al. [40]. One array of 48 stadium shaped devices and another array of 48 circular shaped devices made it possible to measure the resistance of many devices in parallel. The universal conductance fluctuations are averaged out and the weak localization line shape is very clear. The experimental results exhibit a good agreement with (14) and (15).

6. Quantum Chaos in Closed Microstructures: Quantum Dots

In open microstructures many quantum levels, or rather scattering states, play a role simultaneously. It is also of interest to study quantum chaotic systems, where only one or a few levels are important at a given instant. Such systems are closed microstructures also known as quantum dots.

6.1. Coulomb blockade in quantum dots

The main feature of a quantum dot is the Coulomb blockade phenomenon. Because of the smallness of the dot ($L \sim 1\ \mu$m) its capacitance is minute ($C \sim 10^{-16}$ F) and hence the electrostatic charging energy $E_Q = e^2/2C$ associated with one electron is relatively large ($E_Q \sim 0.5$ meV ~ 5 K). At temperatures lower than E_Q the presence of one extra electron on the dot can effectively block the appearance of the next. In transport measurements on the quantum dot in the Coulomb blockade regime it is thus only the last occupied electron state which is probed.

One example of a semiconductor quantum dot is shown in Fig. 6a. The patterned metal gate on top of the GaAs/$Ga_{1-x}Al_xAs$ heterostructure defines a narrow channel with two potential barriers. The electrons can move along the narrow channel (the left lead), tunnel into the region between the barriers (the quantum dot), and then tunnel out again and continue along the channel (the right lead). With the gate voltage V_g the electrostatic energy of the system can be changed. In a simple model of the system the energy E of the dot is a quadratic function of the charge Q on the island: $E = QV_g + Q^2/2C$. Q, however, is quantized in units of the electron charge $-e$: $Q = -Ne$, N being the number of electrons on the dot,

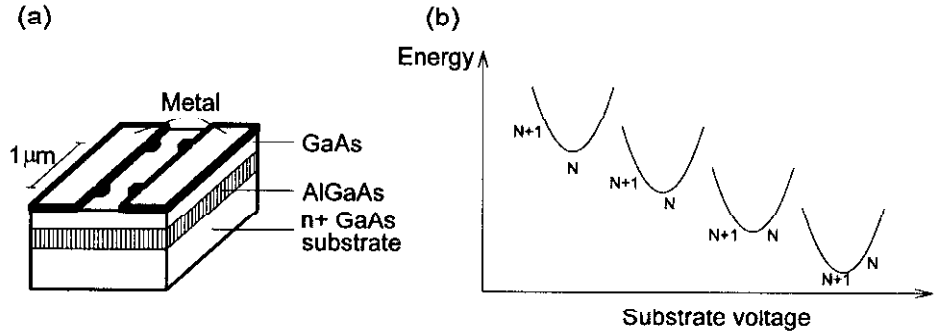

Fig. 6. (a) Schematic drawing of the device structure. The quantum dot is formed between the two barriers in the narrow channel. The density of the 2DEG can be controlled by the substrate voltage V_g (from [11]). (b) The electrostatic energy of the dot as a function of V_g. Only discrete values of charge on the dot is allowed as marked by the dots. In particular, the energies $E(N)$ and $E(N+1)$ are shown.

so only a discrete set of points $E(N)$ on the energy parabola is available for the system. If one particular value of N brings the system close to the bottom of the energy parabola, the Coulomb blockade is effective; it takes too much energy to reach any other state, $E(N) \ll E(N \pm 1)$, whereas if the states N and $N+1$ lie symmetrically around the minimum, the system is at resonance, $E(N) = E(N+1)$, and electrons can flow through the dot. This behavior is sketched in Fig. 6b.

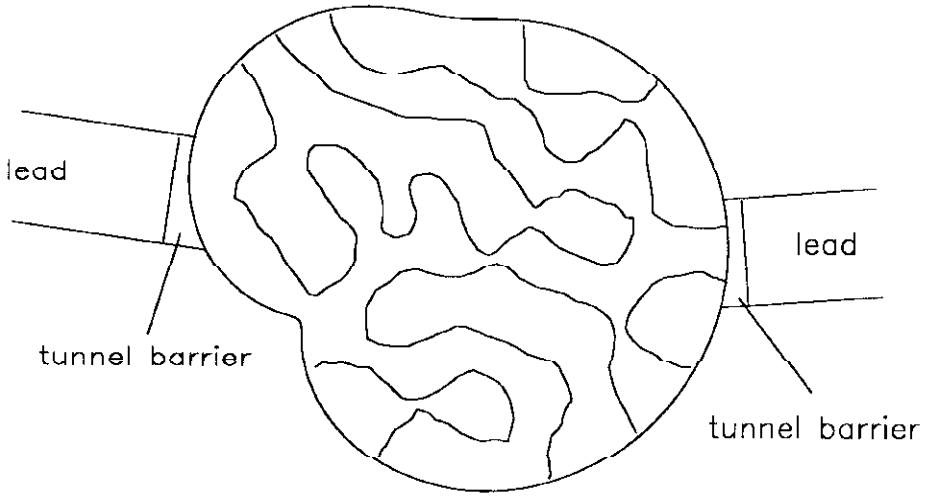

Fig. 7. The model studied to explain the fluctuating peak heights. The leads, the tunnel barriers, and the quantum dot is shown. The lines inside the dot represent the nodal lines of an eigenstate.

In a typical experiment of conductance versus gate voltage a pronounced series of peaks are seen. Two regular features are noted: First, the peaks are (nearly) equidistant. This is related to the constant voltage which is required to accommodate one extra electron in the dot. Second, all the peaks have the same width ($\sim 4kT$). This is because the intrinsic widths of the resonances are much smaller than the temperature, so thermal broadening dominates. One irregular feature is seen: the amplitudes of the peaks vary in a random way. In the following we are going to focus on this phenomenon.

Let us first establish the different energy scales. The largest energy is $E_Q \sim 5$ K. Then follows the single-particle level spacing $\Delta\varepsilon \sim 500$ mK. It is thus possible to achieve $T < \Delta\varepsilon$ so that only one level participates in the resonance. The smallest energy is the level width Γ_λ of a quasi-bound level λ inside the quantum dots. The regime where $\Gamma_\lambda < kT < \Delta\varepsilon < E_Q$ will be denoted the single level regime. Because kT is no longer the smallest energy, we have to generalize the zero-temperature Landauer-Büttiker formula (9) to finite temperature. This is done simply by folding with the derivative $f'(\varepsilon)$ of the Fermi distribution function,

$$G = \frac{2e^2}{h} \int d\varepsilon (-f'(\varepsilon)) \sum_{\alpha,\beta} |t_{\alpha\beta}(\varepsilon)|^2 . \tag{16}$$

At resonance in the single level regime only one level dominates. The sum in (16) therefore reduces to one term. Furthermore, since Γ_λ is very small, $|t|^2$ is described by a very narrow Breit-Wigner resonance. Therefore, $f'(\varepsilon)$ varies slowly as compared to $|t|^2$ and it can be taken outside the integral, which then results in the well known expression for the total area under a Breit-Wigner resonance. G thus becomes [41]

$$G = \frac{2e^2}{h}(-f'(\varepsilon_\lambda)) \frac{\Gamma_\lambda^l \Gamma_\lambda^r}{\Gamma_\lambda^l + \Gamma_\lambda^r} , \tag{17}$$

and the amplitude $G_\lambda^{\max}$ for the resonance due to level λ is

$$G_\lambda^{\max} = \frac{2e^2}{h} \frac{\pi\Gamma}{2kT} \frac{\Gamma_\lambda^l \Gamma_\lambda^r}{\Gamma(\Gamma_\lambda^l + \Gamma_\lambda^r)} \equiv \frac{2e^2}{h} \frac{\pi\Gamma}{2kT} \alpha_\lambda , \tag{18}$$

where Γ is an average value of the collection of conductance peaks under consideration, and where α_λ is introduced as a normalized area of the resonance peak λ. From (17) it is evident that the shapes are determined solely by $f'(\varepsilon)$. In fact, the line shapes are so perfect that the true electron temperature can be determined by fitting with $f'(\varepsilon)$ [11]. From (18) it is clear that the fluctuating peak heights must be understood by analyzing the statistics of Γ_λ^l and Γ_λ^r for a collection of peaks. The main idea is illustrated in Fig. 7: the probability for an electron to tunnel into the dot at a resonance λ is dependent on the amplitude of the eigenfunction near the barrier. If many nodal lines are present in that region, the amplitude is small and tunneling (and hence conductance) is suppressed. If only a few or no nodal lines are present, tunneling is very likely and the conductance is high. The fluctuations in the peak heights are due to the fluctuations in the wave function structures of the individual (quasi-) eigenlevels of the dot. However, these fluctuations are only random if the shape of the dot is irregular. In the following we therefore study a deformable dot. We rely heavily on [16].

6.2. Definition of the deformable dot

The deformed quantum dot is modeled by billiards defined below. A mathematically simple way of defining a continuous deformable family of billiards was introduced by Robnik [42] and Berry and Robnik [43]. It is based on a conformal mapping of the unit disk. To make this paper self-contained and to facilitate the presentation of some new developments of the method we shall briefly describe the technique below.

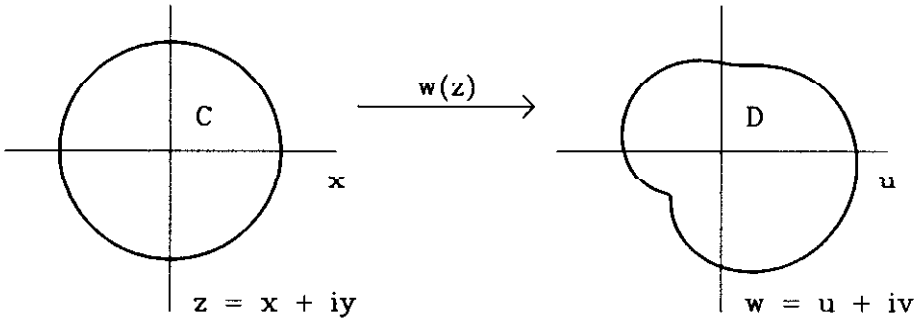

Fig. 8. The deformed billiard $\mathcal{D}$ is the image of the unit disk $\mathcal{C}$ under the mapping $w(z)$, which is conformal ($w'(z) \neq 0, \forall z \in \mathcal{C}$) and area preserving ($\int_{\mathcal{C}} |w'(z)|^2 dz = \pi$).

As shown in Fig. 8, we study a simply connected domain $\mathcal{D}$ with a possibly irregular boundary $\partial\mathcal{D}$ in the uv plane. The interior of the domain is denoted $\mathcal{D}\backslash\partial\mathcal{D}$. The deformed billiard is defined by the infinitely hard wall potential $V(u,v)$ satisfying

$$V(u,v) = \begin{cases} 0, & (u,v) \in \mathcal{D}\backslash\partial\mathcal{D} \\ \infty, & (u,v) \notin \mathcal{D}. \end{cases} \tag{19}$$

Following Robnik [44] we define the shape of $\mathcal{D}$ by a conformal mapping w of the unit disk $\mathcal{C}$ in the xy plane to $\mathcal{D}$ in the uv plane. Parts of the treatment are more conveniently carried out by introducing complex coordinates $z = x + iy$ and $w(z) = u(z) + iv(z)$. The boundary $\partial\mathcal{D}$ in the w plane is thus given as the image $w(\mathcal{C})$ of the boundary of the unit disk $\partial\mathcal{C}$ in the z plane. Throughout this work we study the cubic mapping [43],

$$w(z) = \frac{z + bz^2 + ce^{i\delta}z^3}{\sqrt{1 + 2b^2 + 3c^2}}, \qquad z \in \mathcal{C}, \tag{20}$$

where b, c, and δ are real parameters chosen such that $|w'(z)| > 0$ for $z \in \mathcal{C}$. The normalization in (20) ensures that the area of $\mathcal{D}$ remains π for any value of the parameters. Two sequences of deformed billiards are show in Fig. 9. The cubic form of $w(z)$ is the simplest conformal map resulting in a billiard with no spatial symmetries (see Fig. 9b). Fig. 9a shows even simpler quadratic map ($c = 0$) with reflection symmetry; Robnik and Berry [45] pointed out that such spatial symmetries can prevent a magnetic flux from generating the orthogonal to unitary transition known from random matrix theory [5], hence we maintain the

more general form although the simple quadratic case is sufficient for many of our calculations.

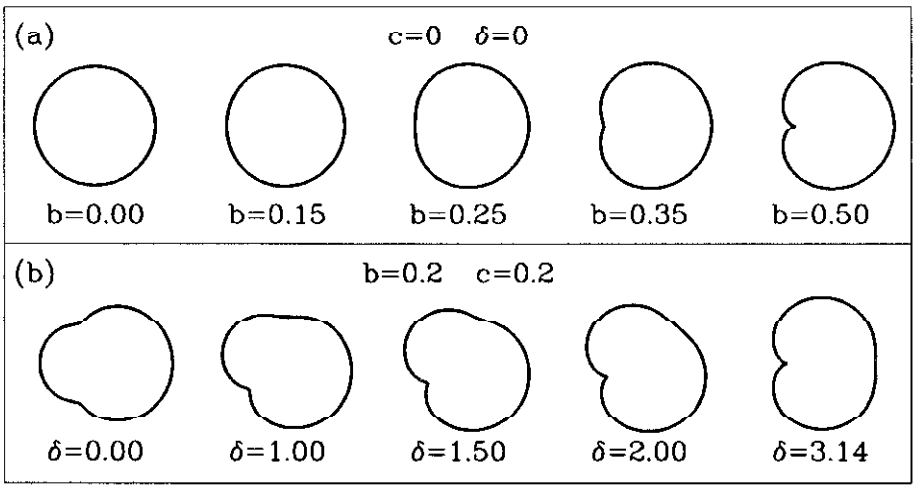

Fig. 9. Two sequences, (a) and (b), of billiard shapes as a function of changing parameters. Sequence (a) was studied by Robnik [42] and sequence (b) by Bruus and Stone [16]. For the very last shape in each sequence $w(z)$ is in fact not conformal. In both of these extreme cases $w'(z) = 0$ just at the point $z = -1$.

6.3. The classical dynamics of the deformed dot

Robnik conducted a thorough study [42] of the classical mechanics of a point mass moving freely in the deformed billiard for the quadratic case ($c = 0$, see Fig. 9a). More recently [46] Hayli et al. have extended his results. Thus in contrast to many previous works on ballistic microstructures in which a discretized version of the Schrödinger equation has been studied [13, 47, 48], in this case one has a detailed knowledge of the classical dynamics of the relevant quantum system. Robnik showed how as a function of b, starting from $b = 0$, the system evolves according to the KAM theorem into a mixed phase-space exhibiting soft chaos and eventually to fully developed chaos. One tool for determining the degree of chaos was to construct the Poincaré surfaces of section for the bounce map and to calculate the Kolmogorov entropy (we will define these notions below). The last large island of stability in the Poincaré section disappears around $b = 0.25$ (the value at which the billiard ceases to be concave) and Robnik originally conjectured that the transition to hard chaos occurred at this value [42]. However recent work has shown that very small islands of stability spawned by the bifurcation of the final stable two-cycle persist up to $b \approx 0.28$, but the precise value of b at which hard chaos sets in is not known. Recently it has been proved [49] that the quadratic billiard at $b = 0.50$ is indeed fully chaotic. In practice, the islands of stability have

negligible weight for $b > 0.25$ and the statistical properties of both the classical and quantum mechanics are consistent with fully developed chaos.

The Poincaré section is constructed by plotting the phase space coordinates of the particle each time it reflects specularly from the boundary of the billiard. The Poincaré section is area-preserving if it is constructed using conjugate canonical variables; a useful set of coordinates for billiards is the arc length σ, measured from the origin to the point the particle hits the boundary, and the tangential momentum $\sin(\chi)$ at this point (χ denotes the angle of incidence) [50]. The surfaces of section clearly reveal how the deformed billiard gets more chaotic as the deformation is increased from zero as in Fig. 9a. Many large stable islands exist at the beginning of the sequence, but as the deformation grows they shrink and vanish sequentially until one obtains the featureless surface of section plot. In contrast, if one starts from a deformed billiard as in Fig. 9b and progresses through further deformations, all the surface of section plots are featureless indicating that all of these billiards are close to hard chaos.

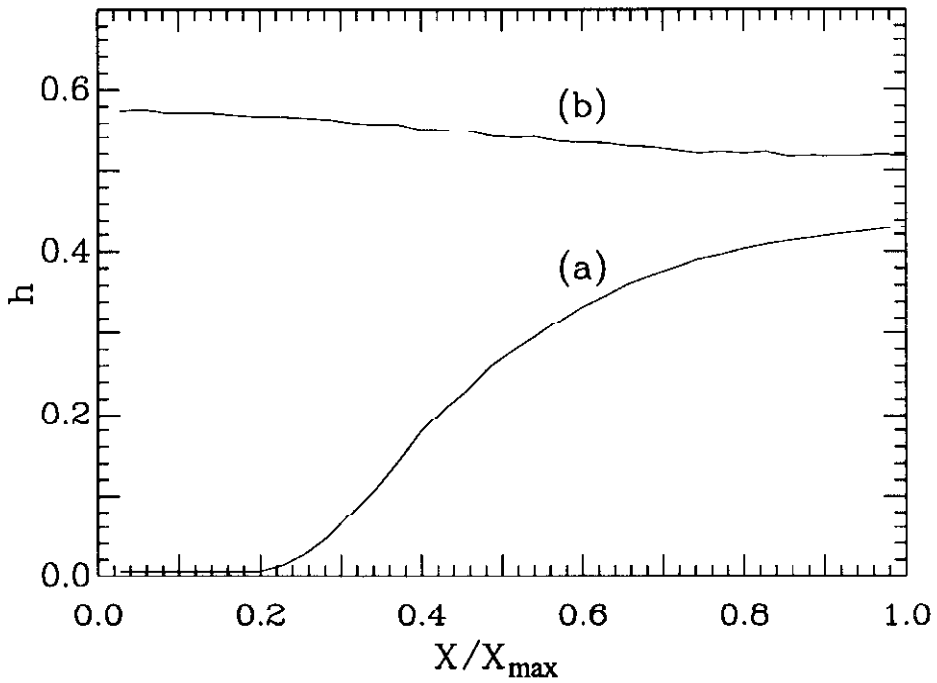

Fig. 10. The Kolmogorov entropy plotted versus the normalized deformation parameter X for the two deformation sequences (a) and (b) in Fig. 9. In (a) $X = b$, and in (b) $X = \delta$.

Quantitative information on the degree of chaos can be obtained by calculating the Lyapunov exponent and the related Kolmogorov entropy [42, 51]. Following Benettin [51], the Lyapunov exponent can be estimated numerically by examining

two trajectories starting at the phase space points $\xi_0^a = \{\sigma_0^a, \sin(\chi_0^a)\}$ and $\xi_0^b = \{\sigma_0^b, \sin(\chi_0^b)\}$ separated by a small distance $d_0 = |\xi_0^b - \xi_0^a| \approx 10^{-10}$. After one bounce the two points ξ_1^a and ξ_1^b are reached, the distance d_1 between them is calculated, and the reduction ratio $\beta_1 = d_0/d_1$ is formed. A new rescaled point ξ_1^{b*} is defined by $\xi_1^{b*} \equiv \xi_1^a + \beta_1(\xi_1^b - \xi_1^a)$. Starting from ξ_1^a and ξ_1^{b*} a second bounce is calculated, and from ξ_2^a and ξ_2^b a new reduction ratio β_2 and a new rescaled point ξ_2^{b*} is formed and the process is repeated. The Lyapunov exponent Λ which generally depends on the initial phase space point can then be calculated as

$$\Lambda(\sigma_0^a, \sin(\chi_0^a)) \;=\; -\lim_{n\to\infty}\left(\frac{1}{t_n}\sum_{i=1}^{n}\ln\beta_i\right), \tag{21}$$

where t_n is the traversal time or the total length in real space of the total n-bounce orbit. From the local measure of chaoticity constituted by Λ, which depends on the initial points in phase space, a global measure, the Kolmogorov entropy h, can be formed:

$$h \;=\; \frac{1}{2\mathcal{L}}\int_{-1}^{1} d(\sin(\chi))\int_0^{\mathcal{L}} d\sigma\;\Lambda(\sigma,\sin(\chi))\,, \tag{22}$$

where $\mathcal{L}$ is the perimeter of the billiard and $(\sigma, \sin(\chi))$ is the initial phase space point. The Kolmogorov entropy h provides a quantitative measure of the degree of chaos in the billiard. In Fig. 10 h is shown for the deformation sequences of Fig. 9. Note how h grows monotonically for the sequence (a), while it is fairly constant and significantly bigger for the sequence (b). Thus, the Kolmogorov entropy calculations indicate that the deformation sequence Fig. 9b is "more chaotic" than the quadratic billiard even at $b = 0.50$, where it is known to be fully chaotic. Of course the K-entropy is essentially an average property of the phase-space and does not allow us to exclude the existence of some very small regions of stability in the sequence, Fig. 9b.

6.4. Quantum mechanics of the deformed billiard

Following Berry and Robnik [43], one can calculate the quantum states of a single particle moving in the interior of the deformed billiard given by (20). The billiard is threaded by an Aharonov-Bohm flux tube of strength $\alpha\Phi_0$ through the origin of the uv plane. Here Φ_0 is the flux quantum h/e and α is a dimensionless real number. Choosing the gauge

$$\mathbf{A}(u,v) \;=\; \frac{\alpha}{2\pi}\Phi_0\left(\frac{\partial f}{\partial v}, -\frac{\partial f}{\partial u}, 0\right), \qquad f \;=\; \frac{1}{2}\ln\left(|z(w)|^2\right), \tag{23}$$

the Schrödinger equation in w coordinates,

$$\frac{1}{2m}(-i\hbar\boldsymbol{\nabla}_w + e\mathbf{A}(w))^2\Psi(w) \;=\; E\Psi(w)\,, \tag{24}$$

becomes the following in the polar coordinates (r,θ) of the xy plane:

$$\boldsymbol{\nabla}^2_{r,\theta}\Psi(r,\theta) - \frac{i2\alpha}{r^2}\partial_\theta\Psi(r,\theta) - \frac{\alpha^2}{r^2}\Psi(r,\theta) + \varepsilon|w'(re^{i\theta})|^2\Psi(r,\theta) \;=\; 0\,, \tag{25}$$

where now the energy ϵ is given in units of $\hbar^2/2mR^2$ and lengths in units of R, R being the radius of the circle $\mathcal{C}$. The spectrum of the Hamiltonian is periodic in α with period 1. Except for the two values $\alpha = 0, 1/2$ for which a real nondiagonal representation of the Hamiltonian can be found, the Hamiltonian is a full complex Hermitian operator. Hence, in terms of random matrix theory [5] Gaussian Unitary Ensemble (GUE) statistics is expected for the level spacing for all α except for values close to 0 and 1/2 at which Gaussian Orthogonal Ensemble (GOE) statistics is anticipated. When focusing on the GUE case we choose $\alpha = 1/4$ to stay as far away as possible from the GOE values.

Thus, using the fact that the deformed billiard is obtained by a conformal map of the unit disk, we may replace the original problem on the irregular domain $\mathcal{D}$ by an equivalent problem on the unit disk moving under a rather simple "potential" proportional to $|w'(re^{i\theta})|^2$. In the simplest cases of Dirichlet or Neumann boundary conditions (denoted DBC and NBC, respectively) the boundary conditions of the equivalent problem are identical to those on the original domain. Since a convenient basis which satisfies these boundary conditions is available (products of Bessel functions, $J_\nu(\gamma r)$, and exponentials, $\exp(il\theta)$) (25) may be expressed as a linear equation in that (infinite) basis which after truncation may be solved numerically. Typically in this study we truncate (25) to the subspace of the 1000 lowest energy Bessel solutions. The dependence of this linear equation on the shape parameters b, c, and δ can be factored out allowing a very efficient numerical method of solution as the shape is varied. To discuss physical properties relating to isolated quantum dots it is reasonable to consider this model with Dirichlet boundary conditions; however, we are interested in fluctuation properties related to conductance. In this case the deformed dot must be coupled to leads (typically through tunnel barriers) and more general boundary conditions must be imposed to describe its scattering resonances.

Therefore, we have to abandon the DBC which are relevant only for closed systems. A partially open system will require not just boundary conditions but also matching conditions for the solutions inside and outside. Such matching conditions can be expressed in terms of any basis set for the region $\mathcal{D}$ which does not cause the wave function to vanish identically (as DBC do). The mathematically simplest alternative choice is Neumann boundary conditions (NBC) for which the normal derivative and hence the particle current vanishes everywhere on the boundary,

$$\mathbf{n}\cdot\boldsymbol{\nabla}\Psi(w) \;=\; 0\,, \qquad w \in \partial\mathcal{D}\,, \tag{26}$$

where $\mathbf{n}$ is the outward pointing normal of the boundary at the point w. For a complete treatment of the quantum mechanics of this problem as well as for a more realistic choice of boundary conditions see [16].

Although the change from DBC to NBC leads to relatively minor changes in the method of solution, the relation between the quantum mechanics and the classical mechanics studied in Section 6.3 becomes less clear since it is natural to associate hard walls in the classical problem with DBC in the quantum problem. Thus, it is of some interest to see if the relation between classical chaos and RMT is independent of this change in the boundary conditions of the quantum problem. The histograms of the level spacing distributions for the NBC case are calculated and χ^2-tests for the GOE and GUE level statistics are performed. The result is shown

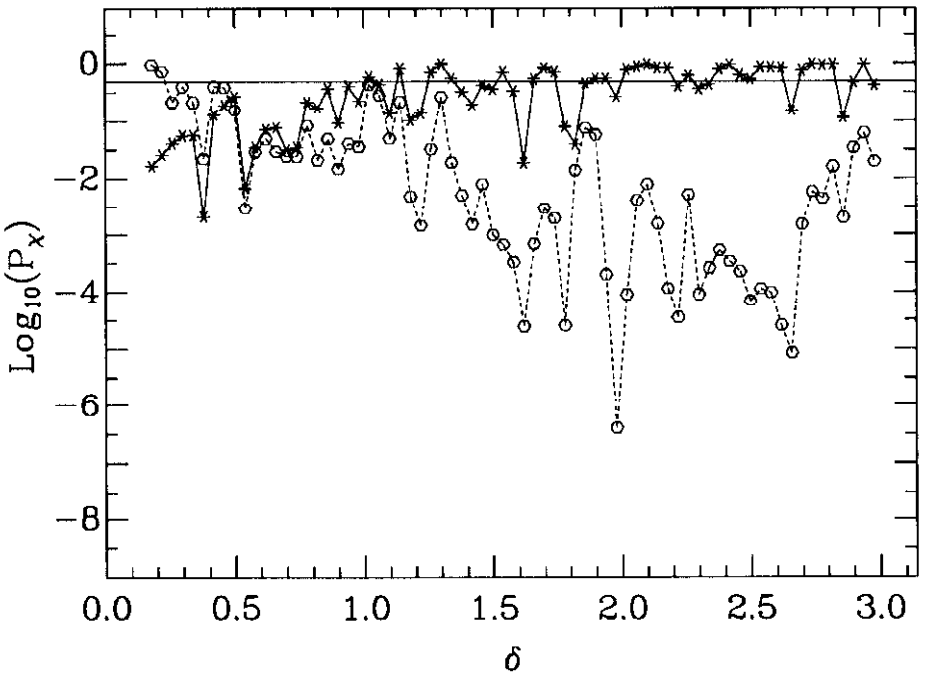

Fig. 11. The χ^2 test for the deformation sequence shown in Fig. 9b in the case of NBC and with an AB-flux of $\frac{1}{4}\Phi_0$. The solid line ($*$) is the test for GUE statistics while the dashed line ($\circ$) is for GOE statistics. The horizontal line is the (logarithm of the) mean value 1/2 around which a successful χ^2 -test ought to fluctuate. Note the rather wide crossover region between the two statistics near the symmetry point $\delta = 0$.

in Fig. 11, where it is seen that the level spacing distributions are well described by GUE statistics, except near the special values of $\alpha = 0, 1/2$. We observe that the crossover region between GOE and GUE statistics near the $\delta = 0$ is quite wide. This might be due to the fact that we are not very deep into the semiclassical regime. Nonetheless the results overall indicate that the correspondence between classical chaos and RMT behavior for the spacing distribution is independent of the boundary conditions.

6.5. Statistics of Coulomb blockade conduction peaks

Fluctuations in the spectrum of quantum dots are not yet easily accessible experimentally. The most striking fluctuation effect evident in the experimental data [11, 12, 15] are fluctuations in the peak height of Coulomb blockade resonances. These fluctuations reflect properties of the quasi-bound states (level-width fluctuations) and not of the spectrum. This contrasts with nuclear scattering resonances in which both spectral and level-width fluctuations are equally accessible. The reason for this difference [13, 15] is that the quantum dot resonances correspond to the ground state energy of the system with $N, N+1, N+2, \ldots$ electrons and

thus include the charging energy e^2/C associated with the addition of a particle. Since this charging energy is approximately constant and is typically an order of magnitude larger than the single-particle excitation energy, $\Delta\varepsilon$ (or more precisely the energy to the first excited state for fixed N) the observed resonances are equally-spaced to a good approximation. In addition, typically $kT \gg \bar{\Gamma}$ (the mean level-width at zero temperature) so the resonances are thermally-broadened to a width $\sim kT$ and only their amplitude reflects the level-width fluctuations. The amplitude fluctuations become maximal when $kT < \Delta\varepsilon$ and only the ground-state contributes to the resonance. In recent experiments [11, 15] $\Delta\varepsilon \sim 0.5$ K so that this single-level regime is accessible. The crossover between multiple-level and single-level tunneling leads to unusual and fluctuating temperature-dependences for the resonances until $kT \ll \Delta\varepsilon$, as was first understood by Meir et al. [52]. In earlier work [13, 14, 15] we have developed a detailed theory of the amplitude fluctuations in the single-level regime assuming that RMT describes the quasi-bound eigenstate fluctuations. Numerical tests of the theory agreed well for the GOE case but not as well for the GUE case [13], and were performed for a disordered model which was assumed to generate chaotic classical dynamics. Here we extend and improve these numerical tests by using the conformal billiard model treated above.

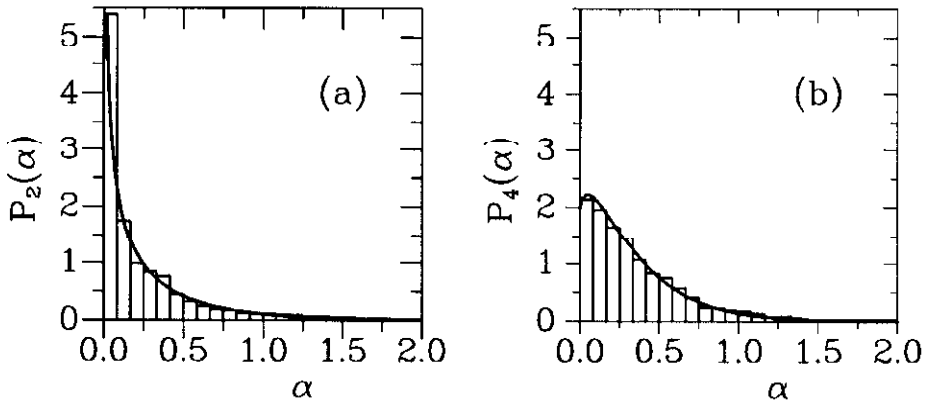

Fig. 12. Predicted distribution of peak amplitudes α in the presence (a) and in the absence (b) of time-reversal symmetry, compared to the numerically generated amplitude distribution obtained with the shape parameters $b = c = 0.2$ and $\delta = \pi/3$.

As before, we model the quantum dot as a deformed billiard accessible by tunneling from leads as shown in Fig. 7. We neglect electron-electron interactions for the following reasons. First, they will add a charging energy which is irrelevant to the level-width fluctuations. Second, although the quasi-bound levels in the presence of electron-electron interactions will surely differ from those in its absence, we do not expect this difference to change their statistical properties (at least in the chaotic case). This concept underlies the universality of RMT and is supported by experimental and theoretical work in nuclear scattering. For example complicated shell-model calculations including the residual nuclear interaction lead to spectra which exhibit RMT statistics [53]. The fact that RMT statistics arise in disordered

or chaotic non-interacting quantum Hamiltonians by no means implies that they occur only when interactions are negligible.

As in nuclear physics [54], one may relate the scattering resonance area α_λ of (18) to the eigenstates $\tilde{\psi}_\lambda$ of the dot in isolation using R-matrix theory. We skip the details here (see [13, 14, 15, 16]) and just state the result that the tunnel amplitude γ_λ^m at the resonance λ is proportional to an overlap integral (known as the reduced width $\tilde{\gamma}_\lambda^m$) between the wave functions in the lead and inside the quantum dot along that part of the perimeter where the tunneling takes place,

$$\gamma_\lambda^m \;=\; \sqrt{P_\lambda}\int_{-W/2}^{+W/2} d\eta_m\, Y(\eta_m)\tilde{\psi}_\lambda(\xi_m^0,\eta_m) \;\equiv\; \sqrt{P_\lambda}\tilde{\gamma}_\lambda^m\,. \tag{27}$$

Here P_λ is the barrier penetration factor, ξ_m denotes the direction parallel to lead m, and η the perpendicular one. $Y(\eta_m)$ is the transverse wave function in the leads (which have width W), and ξ_m^0 is the position of the inner edge of tunnel barrier m. In the experiments two leads are present, the right lead r and the left lead l. The associated level widths $\Gamma_\lambda^{l,r}$ are related to the reduced widths $\tilde{\gamma}_\lambda^{l,r}$ as

$$\Gamma_\lambda^{l,r} \;=\; \frac{\hbar^2 k}{m}|\gamma_\lambda^{l,r}|^2 \;\equiv\; \frac{\hbar^2 k}{m}P_\lambda^{l,r}|\tilde{\gamma}_\lambda^{l,r}|^2\,. \tag{28}$$

The level width will fluctuate from level to level (and for different lead positions for a given level) due to the complicated spatial structure of the chaotic eigenfunctions $\tilde{\psi}_\lambda$ (see Fig. 7). For example, if there happens to be a nodal line near the position of a given lead then the width associated with that level and that lead will fluctuate down. (Note that in the absence of spatial symmetry another lead attached a few wavelengths away will give a completely uncorrelated width for the same level).

As mentioned in Section 6.1, the level-widths are related to the experimentally observed peak amplitudes through (18) for the peak height $G_\lambda^{\max}$. In this discussion we will only treat the case of equal barriers on each side of the dot, and hence $P_\lambda(E)$ will be the same on the left and right. This means that the *average* decay widths to the left and right are equal, $\bar{\Gamma}^l = \bar{\Gamma}^r = \bar{\Gamma}/2$, and we can express α_λ as

$$\alpha_\lambda \;=\; \frac{\Gamma_\lambda^l\Gamma_\lambda^r}{\bar{\Gamma}(\Gamma_\lambda^l+\Gamma_\lambda^r)} \;=\; \frac{|\tilde{\gamma}_\lambda^l|^2|\tilde{\gamma}_\lambda^r|^2}{(|\tilde{\gamma}_\lambda^l|^2+|\tilde{\gamma}_\lambda^r|^2)}\,. \tag{29}$$

The statistics of the peak amplitude fluctuations then follow from those of the reduced partial widths $|\tilde{\gamma}_\lambda|^2$ using (18) and (29).

Assuming that random matrix theory works well in the chaotic regime, one can derive [13] from (29) the probability density $\mathcal{P}_\nu(\alpha)$ of peak areas where $\nu = 2$ for the orthogonal case and $\nu = 4$ for the unitary case. One finds

$$\mathcal{P}_2(\alpha) \;=\; \sqrt{2/\pi\alpha}\,e^{-2\alpha}\,, \tag{30}$$

$$\mathcal{P}_4(\alpha) \;=\; 4\alpha[K_0(2\alpha)+K_1(2\alpha)]\,e^{-2\alpha}\,, \tag{31}$$

where K_n are the modified Bessel functions of the second kind. $\mathcal{P}_2$ and $\mathcal{P}_4$ are plotted in Fig. 12 where they are compared to numerical data obtained by evaluating α in (29) for the 300 lowest wave functions of the conformal model for NBC

in both the GOE and the GUE case. The time-reversal (TR) symmetry-breaking needed to study the GUE case is achieved by adding an AB-flux of one quarter of a flux quantum. In contrast to the results in [13], we find excellent agreement between random-matrix theory and numerical calculation in both the GOE and the GUE case. Note the substantial suppression of small peak amplitudes caused by breaking time-reversal symmetry. This reduces substantially the variance of α, from (30) and (31) one finds $\Delta\alpha_4^2/\Delta\alpha_2^2 = 32/45 \approx 0.71$. For the first experimental measurements of peak height distributions $\mathcal{P}(\alpha)$ see [55, 56].

The effect of a TR-symmetry breaking magnetic field on the distribution and its moments provides perhaps the simplest experimental test of our theory. However, if the suppression of the amplitude fluctuations due to time-reversal symmetry breaking is to be cleanly observable, then the magnetic field necessary to induce the GOE-GUE transition must be small compared to that needed for Landau level formation. Landau level formation strongly suppresses the fluctuations [57]; the classical analogue of this effect is the suppression of chaos by the formation of stable skipping orbits [58]. We estimate the magnetic field scale for TR-symmetry breaking by adapting an argument first put forward (to our knowledge) by Berry and Robnik [43] TR-symmetry is broken first not by the dynamic effect of the field but by its effect on the phase of the wave functions (essentially the Aharonov-Bohm effect). Therefore, in estimating the TR-symmetry breaking scale we may neglect the dynamic effect of the field entirely. Gutzwiller's trace formula [4] implies that structure in the spectrum on the scale of the level spacing $\Delta\varepsilon$ arises from periodic orbits of period $T \approx \hbar/\Delta\varepsilon$. A magnetic field will change the action (in units of $\hbar$) of such orbits by $BA_T/(h/e)$, where A_T is the area enclosed by the periodic orbit of period T in the chaotic case. The time-reversed orbit will of course enclose area $-A_T$ and their relative phases will be shifted by the order of unity when $BA_T \approx (h/e)$, breaking TR-symmetry. Thus the critical field B_c for TR-symmetry breaking is given by $B_c \sim (h/e)/A_T$ and one needs only to estimate A_T. Berry and Robnik [43] treated the case of an A-B flux as above and then evaluated the mean-squared winding number for such orbits in the chaotic limit. Their results can be extrapolated to a uniform field simply by assuming that a typical (positive or negative) area of order A (the area of the dot) is enclosed with each circuit. With this modest assumption the TR-symmetry breaking flux

$$\Phi_c = B_c A \sim [\Delta\varepsilon\sqrt{A}/\hbar v_f]^{1/2}(h/e)\,. \tag{32}$$

Although in the experiments the dot is not isolated as assumed in this argument, the condition $\bar{\Gamma} \ll \Delta\varepsilon$ ensures that electrons remain in the dot long enough for the argument to still apply. The ratio of this field to the field at which the cyclotron radius becomes of the order of the radius of the dot scales like $N^{-3/4}$, where N is the number of electrons; so in dots containing a few hundred electrons TR-symmetry breaking occurs at a field one to two orders of magnitude smaller than that needed for edge-state formation. In the experimental systems of interest this corresponds to a field of order a few times 10 mT. Thus, the statistical effect of time-reversal symmetry breaking predicted by our theory should be observable experimentally.

6.6. Optimal experimental setup

To obtain the most direct experimental verification of the theoretical results presented here and in earlier work, it is desirable to fabricate a quantum dot with a variable shape. In current experimental systems only a few tens of Coulomb blockade peaks are measured in a given dot and these are superimposed on a significant background which complicates the comparison of the height of widely-separated peaks. Thus obtaining reasonable statistics (e.g. roughly one hundred peak amplitudes) is very difficult. It is possible to use the magnetic field itself as an external control parameter causing peak amplitude fluctuations [15], but this only allows one to collect statistics for the GUE case.

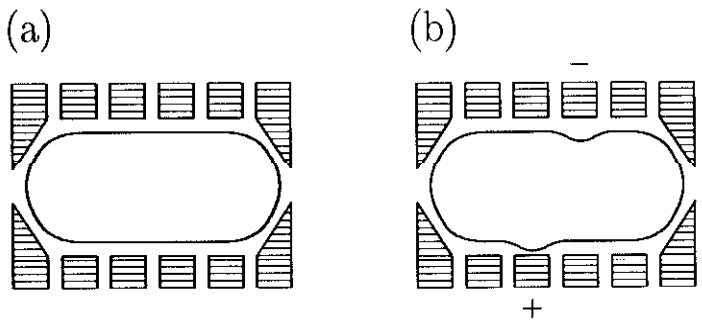

Fig. 13. A top view of a gated heterostructure. The gate is split into twelve teeth. The two pairs at the ends form quantum point contacts leading to the surrounding two-dimensional electron gas. The remaining eight teeth define the shape of the quantum dot. In situation (a) all the interior gates have the same voltage. In (b) one gate has a slightly higher voltage and another slightly lower thereby deforming the dot while maintaining its area. The regions close to the quantum point contacts are essentially unaffected by this action.

Therefore, we suggest that an optimal heterostructure for tests of RMT statistics would consist of a dot formed by multiple teeth-like gates (see Fig. 13). By changing the voltages slightly on the inner gates of this structure it should be possible to realize a whole range of shapes without affecting the region near the quantum point contacts defining the tunnel barriers to the surrounding two-dimensional electron gas. It would then be possible to follow a given peak as a function of shape and collect statistics without the complication of background variation, both in the presence and absence of a magnetic field. Since the magnetic field would not be the control parameter it would also be possible to map out the GOE to GUE transition. For further experimental and theoretical developments along these lines see [56, 59].

7. Concluding Remarks

In these lectures we have seen the first examples of experiments in semiconductor microstructures demonstrating that the quantum chaos concepts developed theoretically are important for understanding transport phenomena in condensed

matter systems. At this stage the primary concern has been to demonstrate the existence of any effects of chaos in the microstructures. The effects mentioned in the lectures form such a demonstration, and we have seen that the combination of the semiclassical approach and chaos theory has proved useful in the interpretation of complicated quantum phenomena in the ballistic regime, such as conductance fluctuations and weak localization. Also, we have seen how chaos concepts have led to the explanation of the fluctuating peak heights in the Coulomb blockade oscillations.

After taking these initial steps the microstructure research in the near future can focus on answering more fundamental questions. For example, the phase coherence length is limited in real experiments. How short can it be without suppressing chaos effect completely? And what is the effect of the unavoidable loss of phase coherence for long classical paths? Furthermore, so far only single particle chaos effects have been studied, but it seems reasonable to believe that the microstructures after some refining of the present day experimental technique may serve as an ideal laboratory for investigating chaos in interacting many particle systems. In that case, microstructure research may become a source of inspiration for further development of general chaos theory.

Acknowledgments

It is a pleasure to thank Doug Stone, Harold Baranger, and Charlie Marcus for stimulating and very helpful discussions. This work has been supported by the Danish Natural Science Research Council under grant no. 11-0271.

Bibliography

1. For review of the physics of semiconducting mesoscopic devices see C. W. J. Beenakker and H. van Houten, Solid State Phys. **44**, 1 (1991). Reviews of some aspects of quantum chaos in nanostructures can be found in Chaos **3**, (1993).
2. B. L Altshuler and B. I. Shklovskii, Zh. Eksp. Teor. Fiz. **91**, 220 (1986) [Sov. Phys.-JETP **64**, 127 (1986)].
3. N. Argaman, Y. Imry, and U. Smilansky, Phys. Rev. B **47**, 4440 (1993).
4. For a recent review see M. C. Gutzwiller, *Chaos in Classical and Quantum Mechanics*, Springer Verlag, New York, 1990.
5. M. L. Mehta, *Random Matrices and the Statistical Theory of Energy Levels*, Academic, New York, 1991.
6. O. Bohigas, M.-J. Giannoni, and C. Schmit, Phys. Rev. Lett. **52**, 1 (1984).
7. R. A. Jalabert, H. U. Baranger, and A. D. Stone, Phys. Rev. Lett. **65**, 2442 (1990)
8. C. M. Marcus, A. J. Rimberg, R. M. Westervelt, P. F. Hopkins, and A. C. Gossard, Phys. Rev. Lett. **69**, 506 (1992).
9. M. W. Keller, O. Millo, A. Mittal, D. E. Prober, and R. N. Sachs, Surf. Sci. **305**, 501 (1994).
10. H. U. Baranger, R. A. Jalabert, and A. D. Stone, Phys. Rev. Lett. **70**, 3876 (1993)
11. U. Meirav, M. A. Kastner and S. J. Wind, Phys. Rev. Lett. **65**, 771 (1990).
12. L. P. Kouwenhoven et al., Z. Phys. B **85**, 367 (1991).
13. R. A. Jalabert, A. D. Stone, and Y. Alhassid, Phys. Rev. Lett. **68**, 3468 (1992).
14. A. D. Stone, R. A. Jalabert, and Y. Alhassid, in: Springer Series in Solid-State Sciences, Vol 109, Eds. H. Fukuyama and T. Ando, Springer, Berlin, p. 39, 1992.
15. A. D. Stone and H. Bruus, Physica B **189**, 43 (1993), and Surf. Sci. **305**, 490 (1994).
16. H. Bruus and A. D. Stone, Phys. Rev. B **50**, 18275 (1994).

17. V. N. Prigodin, K. B. Efetov, and S. Iida, Phys. Rev. Lett. **71**, 1230 (1993).
18. H. U. Baranger and P. A. Mello, unpublished.
19. C. W. J. Beenakker, R. A. Jalabert and J.-L. Pichard, unpublished.
20. H. L. Störmer, R. Dingle, A. C. Gossard, W. Wiegman, and M. D. Sturge, Solid State Commun. **29**, 705 (1979).
21. D. C. Tsui, H. L. Störmer, and A. C. Gossard, Phys. Rev. Lett. **48**, 1559 (1982).
22. B. J. van Wees et al, Phys. Rev. Lett. **60**, 848 (1988).
23. F. Stern and S. Das Sarma, Phys. Rev. B **30**, 840 (1984).
24. P. W. Anderson, E. Abrahams, and T. V. Rammakrishnan, Phys. Rev. Lett. **43**, 718 (1979).
25. L. P. Gorkov, A. I. Larkin, and D. E. Khmelnitskii, Pis'ma Zh. Eksp. Teor. Fiz. **30**, 248 (1979) [JETP Lett. **30**, 228 (1979)].
26. A. I. Larkin and D. E. Khmelnitskii, Usp. Fiz. Nauk **136**, 536 (1982) [Sov. Phys. Usp. **25**, 185 (1982)].
27. S. Chakravarty and A. Schmid, Phys. Rep. **140**, 193 (1986).
28. D. Yu. Sharvin and Yu. V. Sharvin, Pis'ma Zh. Eksp. Teor. Fiz. **34**, 285 (1982) [JETP Lett. **34**, 272 (1982)].
29. B. L. Altshuler, A. G. Aronov, B. Z. Spivak, and Yu. V. Sharvin, Pis'ma Zh. Eksp. Teor. Fiz. **35**, 476 (1982) [JETP Lett. **35**, 588 (1982)].
30. R. Landauer, IBM J. Res. Dev. **1**, 223 (1957).
31. M. Büttiker, Phys. Rev. Lett. **57**, 1761 (1986).
32. P. A. Lee and A. D. Stone, Phys. Rev. Lett. **55**, 1622 (1985).
33. B. L. Altshuler, Pis'ma Zh. Eksp. Teor. Fiz. **41**, 530 (1985) [JETP Lett. **41**, 648 (1985)].
34. P. A. Lee, A. D. Stone, and H. Fukuyama, Phys. Rev. B **35**, 1039 (1987).
35. P. A. Lee, Physica **140A**, 169 (1986).
36. S. Washburn, Chapter 1 in *Mesoscopic phenomena in solids*, eds. B. L. Altshuler, P. A. Lee, R. A. Webb, North-Holland, New York, 1991.
37. C. J. B. Ford et al. Phys. Rev. Lett. **62**, 2724 (1989).
38. C. M. Marcus et al. Phys. Rev. Lett. **69**, 506 (1992).
39. H. U. Baranger, D. P. DiVincenzo, R. A. Jalabert, and A. D. Stone, Phys. Rev. B **44**, 10637 (1991).
40. A. M. Chang, H. U. Baranger, L. N. Pfeiffer, and K. W. West, Phys. Rev. Lett. **73**, 2111 (1994).
41. C. W. J. Beenakker, Phys. Rev. B **44**, 1646 (1991).
42. M. Robnik, J. Phys. A **16**, 3971 (1983).
43. M. V. Berry and M. Robnik, J. Phys. A **19**, 649 (1986).
44. M. Robnik, J. Phys. A **17**, 1049 (1983).
45. M. Robnik and M. V. Berry, J. Phys. A **19**, 669 (1986).
46. A. Hayli, T. Dumont, J. Moulin-Ollagnier, and J.-M. Strelcyn, J. Phys. A **20**, 3237 (1987).
47. A. Szafer and B. L. Altshuler, Phys. Rev. Lett. **70**, 587 (1993)
48. B. D. Simons and B. L. Altshuler, Phys. Rev. Lett. **70**, 4063 (1993) and Phys. Rev. B **48**, 5422 (1993).
49. R. Markarian, Nonlinearity **6**, 819 (1993).
50. M. V. Berry, Eur. J. Phys. **2**, 91 (1981).
51. G. Benettin and J.-M. Strelcyn, Phys. Rev. A **17**, 773 (1978).
52. Y. Meir, N. Wingreen and P. A. Lee, Phys. Rev. Lett. **66**, 3048 (1991).
53. T. A. Brody, J. Flores, J. B. French, P. A. Mello, A. Pandey, and S. S. M. Wong, Rev. Mod. Phys. **53**, 385 (1981).
54. A. M. Lane and R. G. Thomas, Rev. Mod. Phys. **30**, 257 (1958).
55. A. M. Chang, H. U. Baranger, L. N. Pfeiffer, K. W. West, and T. Y. Chang, Phys. Rev. Lett. **76**, 1695 (1996).
56. J. A. Folk et al., Phys. Rev. Lett. **76**, 1699 (1996).
57. R. A. Jalabert and A. D. Stone, unpublished.
58. M. Robnik and M. V. Berry, J. Phys. A **18**, 1361 (1985).
59. H. Bruus, C. H. Lewenkopf, and E. R. Mucciolo, Phys. Rev. B **53**, 9968 (1995).